

Final Draft
of the original manuscript:

Gabrisch, H.; Stark, A.; Schimansky, F.-P.; Wang, L.; Schell, N.;
Lorenz, U.; Pyczak, F.

**Investigation of carbides in Ti–45Al–5Nb–x C alloys ($0 \leq x \leq 1$) by
transmission electron microscopy and high energy-XRD**

In: Intermetallics (2012) Elsevier

DOI: 10.1016/j.intermet.2012.09.023

**Investigation of Carbides in Ti-45Al-5Nb-xC alloys ($0 \leq x \leq 1$) by Transmission
Electron Microscopy and High Energy-XRD**

Heike Gabrisch*, Andreas Stark, Frank-Peter Schimansky, Li Wang, Norbert Schell,
Uwe Lorenz, Florian Pyczak

*Institute of Materials Research, Helmholtz-Zentrum Geesthacht, Max-Planck-Str.1, 21502
Geesthacht, Germany*

Abstract

The mechanical properties of γ -TiAl based alloys are often improved through alloying with niobium and carbon. Depending on composition and heat treatment the details of carbon distribution and the resulting consequences on mechanical properties vary greatly.

Here we present a study of the microstructure of Ti-45Al-5Nb alloys (in at.-%) with the addition of 0.5 – 1 at.-% of carbon. We use electron diffraction accompanied by energy dispersive spectroscopy and imaging in the TEM to characterize carbides. These studies are complemented by high-energy x-ray diffraction experiments using synchrotron radiation and by scanning electron microscopy. Carbides are identified in significant numbers in the alloys containing 1 and 0.75 at.-% of carbon but only rarely at 0.5 at.-% C. Our results show that in these alloys carbon in solid solution has a stronger effect on hardness than carbide precipitation.

Keywords : *A. Intermetallics, ternary alloy systems, B. precipitates, solid solution hardening, F. diffraction (electron, x-ray)*

*corresponding author

Tel +49 4152 87-2540

e-mail : heike.gabrisch@hzg.de

1. Introduction

γ -TiAl based alloys are potential candidates for high strength applications at high temperatures, for example in aircraft engines. The mechanical properties of γ -TiAl based alloys can be improved through alloying with niobium and carbon. Nb stabilizes the β phase and segregates to dendritic primary β phase during solidification but it has little effect on the amount of α_2 and γ phase [1-3]. Nb is evenly distributed in the α_2 and γ phases and preferentially replaces Ti atoms on regular lattice sites [2, 4-6]. Carbon on the other hand stabilizes the α phase. Both C and Nb increase the eutectic temperature of the alloy [7, 8]. The smaller carbon atoms occupy interstitial sites in γ and α_2 phases [9] until the formation of carbides begins above a critical carbon concentration. This critical concentration, or in other words the solubility limit for carbon, is different in the γ and α_2 phases and depends on alloy composition and on thermal history. In general the strengthening effect of carbon may be attributed to solid solution hardening of the matrix phases or to precipitation hardening which has important implications on the alloy behaviour at service temperature.

In Ti-Al alloys two types of carbides are known, Ti_2AlC with a hexagonal lattice (H-phase) and Ti_3AlC with a cubic Perovskite structure (P-phase). Both carbides exist in a carbon deficient form with respect to their 'ideal' stoichiometry determined by the crystal structure formula. Both types of carbide host carbon atoms in octahedral coordination surrounded by Ti atoms [10-13]. According to literature, the H-phase is the stable high temperature phase while the P-phase forms at lower temperatures and is metastable [9, 14, 15].

Effective precipitation hardening requires the presence of small and densely spaced precipitates. Precipitation hardening in the form of P-phase particles in TiAl alloys has been reported by Christoph et. al and Tian and Nemoto [16, 17]. In other studies the improvement of mechanical properties has been attributed to solid solution hardening because no precipitates have been detected [18, 19] or because the observed precipitates had no beneficial effect on the alloy behaviour due to large particle size, instability at high temperature or low strength at low strain rate in comparison to the carbon free alloy [20-22]. The carbon solubility limit of the alloy and its thermal history are obviously important factors that determine whether carbides are formed. Menand et. al and more recently Scheu et. al used atom probe investigations to measure the amount of carbon dissolved in α_2 and γ phases in different alloys [23, 24]. Their results show that the solubility limit in γ -phase lies by an order of magnitude below that of the α_2 phase, and that 250 at-ppm (Menand) or 0.25 at.-%

(Scheu) of C are soluble in γ -phase. The addition of Nb to binary TiAl alloys seems to increase the solubility for carbon. For example P-type carbides have been observed in Ti-48.5Al-0.5C but not in Ti-45Al-5Nb-0.5C [17-19, 23, 25, 26] (all alloy compositions are given in at.-% throughout). P-type and H-type carbides were observed in the ternary alloys Ti-48.5Al-2.1Nb with 600-700 ppm of carbon while only P-type carbides were reported for Ti-46.6Al-1.4Mn with 0.3 at.-% of carbon [14, 27].

In an effort to investigate details of carbide formation in ternary Ti-Al-Nb alloys we study the microstructure of Ti-45Al-5Nb alloys with the addition of 0.5 – 1 at.-% of carbon. We use electron diffraction in a Transmission Electron Microscope (TEM) accompanied by energy dispersive spectroscopy (EDS) to characterize particles embedded in the Ti-Al matrix. These studies are complemented by imaging in a scanning electron microscope (SEM) and by high-energy x-ray diffraction experiments using synchrotron radiation (HERXD). We show that carbides of the hexagonal Ti_2AlC phase and of the cubic Ti_3AlC phase are present at carbon contents ≥ 0.75 at.-%. At 0.5 at.-% of carbon there is evidence for the presence of P-type carbides.

2. Experimental

Ti-45Al-5Nb alloys with carbon additions of 0.5 – 1.0 at.-% were produced in house following a powder metallurgical (PM) route that has been published in detail in [28]. Starting materials were pure elements and titanium carbide (TiC). These were molten into buttons by plasma arc melting in a water-cooled copper crucible. Each button was re-molten four times to ensure chemical homogeneity. The powders were produced by Plasma Melting Induction Guiding Gas Atomization (PIGA). Great caution was taken to prevent the up-take of impurity atoms during processing (such as O, N, or additional C). The amount of oxygen and nitrogen was monitored using the LECO melt extraction system TC436. Powder particles with diameters ≤ 180 μm were filled into titanium (Ti) capsules of 63 mm diameter and 150 mm length. After filling, the capsules were degassed, sealed, and compacted by HIPing at 1250 °C under 200 MPa for 2 h.

Specimens for High-Energy X-Ray Diffraction experiments and Scanning Electron Microscopy were cut from the HIPed rods. Specimens for SEM imaging were mechanically ground and polished followed by electrochemical polishing with a solution of perchloric acid in methanol. Secondary (SE) and backscattered electron (BSE) images, Energy Dispersive Spectrum (EDS) mappings and Electron Back Scattered Diffraction mappings (EBSD) were recorded in the SEM for evaluation with respect to grain size, phase fraction and carbon

distribution. Imaging and mapping were performed in the Leo Gemini 1530 and in the Zeiss Auriga respectively. Phase fractions were determined by Rietveld analysis of XRD patterns, by the line intercept method on SEM images, and by analysis of EBSD mappings. The Rietveld refinement was performed using ideally composed stoichiometric phase-models, i.e. γ -TiAl, α_2 -Ti₃Al and H-Ti₂AlC, because it is not known how Nb distributes onto the different lattice sites. This may introduce a systematic error in the obtained phase fractions but should not obscure trends in the correlation between carbon content and phase fractions. In the analysis of the EBSD mappings the γ phase, that has only a very little tetragonality, was represented by an fcc unit cell. This was necessary because the non-equivalent orientations of the tetragonal γ -phase were not distinguished clearly which introduced unnecessary scatter in the EBSD-mappings. In the evaluation of EBSD data a cut-off radius (minimal grain size) was introduced to avoid meaningless data (grains too small to exist or smaller than observed experimentally). In most cases grains with sizes below this cut-off radius ($R = 0.5\mu\text{m}$ and $1.0\mu\text{m}$) are probably mis-indexed areas belonging to the surrounding larger grain. Thus, it seems justified to exclude these areas from the determination of the average grain sizes. Grain size measurements (average diameter) of γ and α_2 grains were performed on SEM images by the line intercept method using a $3\mu\text{m} \times 3\mu\text{m}$ grid (about 760 grains evaluated per alloy).

For Transmission Electron Microscopy discs of 2.3 mm diameter were drilled out of 500 μm thick slices that were cut perpendicular to the rod length. The discs were ground manually to about 150 μm thickness followed by jet polishing at $-39\text{ }^\circ\text{C}$ with a solution of 18 ml perchloric acid in 430 ml methanol and 250 ml 2-buthanol. The TEM specimens were investigated for the presence of carbon rich precipitates by a combination of imaging, electron diffraction and (qualitative) energy dispersive spectroscopy in a Jeol CM 200 TEM operated at 200kV and in the C_s corrected FEI Titan 3010 TEM operated at 300kV. The software package JEMS was used to simulate high-resolution TEM images for comparison to experimental ones.

The Vickers macro hardness was measured with a load of 20 kg (HV 20) on sections cut parallel (L) and perpendicular (Q) to the rod length.

High-energy X-ray diffraction experiments were carried out at the HZG beamline HEMS at the Deutsches Elektronen-Synchrotron (DESY). Samples with a diameter of about 4 mm were measured in transmission geometry using a beam cross section of 0.5 mm x 0.5 mm. High-energy x-rays having a photon energy of 87 keV, corresponding to a wavelength of $\lambda = 0.1425\text{ \AA}$, were used to penetrate the specimens. The resulting Debye-Scherrer diffraction rings were recorded on a Mar345 image plate detector with an exposure time of 4 seconds.

Conventional diffraction patterns were generated by an azimuthal integration of the Debye-Scherrer rings. Lattice parameters and phase fractions were determined by Rietveld analysis.

In the following text the properties of the alloys are solely classified by their carbon content, therefore we refer to the specimens as carbon-free (Ti-45Al-5Nb), 0.5% alloy (Ti-45Al-5Nb-0.5C), 0.75% alloy (Ti-45Al-5Nb-0.75C) and 1% alloy (Ti-45Al-5Nb-1C).

3. Results

3.1 Microstructure

All alloys show a globular, almost equi-axed grain structure consisting of γ and α_2 grains. Occasionally large lamellar ($\alpha_2+\gamma$) colonies are observed whereby the occurrence rate of the colonies decreases with increasing carbon content. These colonies are irregularly distributed and sometimes ill defined. Examples for the two-phase microstructure, for regions of large lamellar colonies and for ill defined lamellar regions are given in Fig.1. Only regions without lamellar colonies were chosen for the microstructural characterization of grain size and phase fractions by SEM. The characterization of carbides was accomplished by TEM and HEXRD.

3.1.1 Grains Size

In all alloys γ grains are larger than α_2 grains. The largest average grain size for both phases is found in the carbon free alloy with $4.4\pm 0.06\ \mu\text{m}$ and $2.2\pm 0.06\ \mu\text{m}$ for γ and α_2 phase respectively. Upon addition of 0.5% C the grain sizes decrease to minimum values of $3.9\pm 0.06\ \mu\text{m}$ and $2.0\pm 0.06\ \mu\text{m}$ for γ and α_2 respectively. At higher carbon levels the grain sizes grow again. The grain sizes increase to values around $4.2\pm 0.06\ \mu\text{m}$ for γ and $2.2\pm 0.06\ \mu\text{m}$ for α_2 at 0.75 and 1% of carbon, close to the initial size. Interestingly no difference is observed between the grain sizes at carbon contents of 0.75 and 1.0 at.-%.

3.1.2 Phase fraction

The volume fractions of α_2 and γ phases were measured to monitor trends in the amount of phases with increasing carbon content. The results for the amount of γ phase with carbon content are shown in Fig. 2. A comparison of all methods applied does not reveal a clear trend among the alloys containing different amounts of carbon. For example the amount of γ phase determined by Rietveld increases slightly from 77 vol.-% in the C-free alloy to 83 vol.-% (0.5% C), 81 vol.-% (0.75% C), and 82 vol.-% (1.0% C) in the carbon containing alloys. This is roughly in agreement with the amount of γ phase fraction determined from EBSD-mappings. On the other hand a decrease in the γ phase fraction with increasing carbon content was found by quantitative evaluation of SEM micrographs. In the 1% alloy small amounts of

carbides were detected. Based on ratios of diffracted intensities these were estimated to 1.7 vol.-% of H-phase and 0.1 vol.-% of P-phase, see section 3.2.

3.2 HEXRD- results

An overview of the recorded HEXRD spectra is shown in Fig. 3a. All prominent diffraction peaks can be indexed as either α_2 or γ phase. In the spectrum of the 1 % alloy additional small peaks of a third phase appear (see arrows in Fig. 3a). These belong to the hexagonal phase Ti_2AlC . A smaller angular range of the spectra is enlarged in Fig. 3b where the peak positions of the major α_2 and γ phases and of the minor H-type and P-type carbide phases are marked. In the 1 % alloy small diffraction intensities of the H-phase can be detected near $|q|= 2.37$ and $|q|= 2.75$. Additionally, weaker intensities of the P-phase are observed near $|q|= 2.63$ and 3.03 . At close inspection peaks of both phases can be detected in the 0.75 % alloy as well. For the 1 % alloy the amounts of phases determined from relative diffracted intensities are 80.8 vol.-% of γ , 17.4 vol.-% of α_2 , 1.7 vol.-% of H-phase, and 0.1 vol.-% of P-phase. The lattice parameters calculated from the peak positions are : $a = 4.144 \text{ \AA}$ for the P-phase; $a = 3.06 \text{ \AA}$ and $c = 13.63 \text{ \AA}$ for the H-phase.

The influence of carbon on the lattice parameters of $\gamma\text{-TiAl}$ and $\alpha_2\text{-Ti}_3\text{Al}$ is illustrated in Fig. 3c showing a different angular range of the spectra. From zero to 0.75 at.-% of C the positions of γ and α_2 peaks move to smaller scattering vectors q with increasing carbon content (Fig. 3c). This corresponds to an expansion of the γ and α_2 lattice parameters by about 0.5 %. The expansion reaches a maximum at 0.75 at.-% of C. At 1 at.-% of C a slight decrease of lattice parameters is observed. The overall behaviour is summarized in Fig. 4, where the unit cell volumes are plotted over carbon content for α_2 and γ phases. Maxima are observed for both phases at 0.75 at.-% of carbon, the largest increase in unit cell volume is observed for the α_2 phase.

3.3. Hardness

The results of the hardness measurements are displayed in Fig. 5. The sizes of the individual imprints of the pyramidal diamond indenter range between 0.30 - 0.31 mm (6 measurements per specimen, standard deviation 0.01-0.03 mm) and compare to average grain sizes of 3.9 to $4.4 \pm 0.06 \mu\text{m}$ for γ -phase and 2.0 to $2.2 \pm 0.06 \mu\text{m}$ for α_2 phase. In Fig. 5 it can be seen that the hardness increases almost linearly with carbon content from 0 up to 0.75 at.-% C. In the 0.5% alloy the hardness has increased by almost 14% from 334 HV in the carbon

free alloy to 380 HV. Carbon additions above 0.75 at.-% C do not affect the measured hardness values indicating that a plateau has been reached. This trend is similar to the change of lattice parameters with carbon content described above.

3.4 Carbide morphology and distribution

The characterization of carbide precipitates by SEM or TEM is hampered by the preferred dissolution of carbides during specimen preparation using solutions of perchloric acid. An illustration is given in Fig. 6a showing the edge of a TEM foil. The foil is perforated by a network of small and large holes measuring up to 5 μ m in size. The image is taken of the 1% alloy where the highest amount of carbides has been measured by HEXRD. In Fig. 6b a TEM image of the same specimen shows a precipitate that is dissolved at the center. It can be seen that the dissolution starts from the core of the particle and not from the interface between particle and matrix. Analysis of experimental electron diffraction patterns of particles resembling the one in Fig. 6b confirms the hexagonal crystal structure of the Ti₂AlC phase. In Fig. 6c an SEM image is shown together with an EDS scan across an H-type particle. An elevated carbon content in the precipitate is confirmed in the EDS scan.

H-type carbides are observed by TEM in the 0.75% alloy and in the 1 % alloy. The precipitates are typically located at triple junctions between grains and have a large size of up to 1 μ m in diameter. They have a compact, partly faceted shape that is truncated by the dimension of the TEM foil. The density of H-type carbides is much higher in the 1 % alloy than in the 0.75 % alloy. This is illustrated by a comparison between the SEM images in Fig. 7 (1 % C) and Fig. 8 (0.75 % C). Due to selective etching of carbides during electrolytic polishing the positions of former carbides appear as etch pits in the SEM micrographs.

In Fig. 7 of the 1% alloy the same area of the specimen is imaged in SE and a BSE mode in the SEM. In Fig. 7a (SE mode) holes that have formed by dissolution of carbide precipitates are clearly recognized. In Fig. 7b taken in BSE mode it can be seen that these holes decorate the boundaries of larger regions that comprise several grains. For comparison a significantly lower number of particles/etch pits is observed in the SEM image of the 0.75% alloy shown in Fig. 8. TEM micrographs of an H-type particle in the 0.75% alloy observed in bright field and dark field condition using a reflection of the hexagonal H-phase are shown in Fig. 9 together with the corresponding diffraction pattern.

P-type carbides are observed in the alloys with 0.75 and 1 at.-% of carbon in form of small, lens shaped particles located in the boundary of γ grains. An example is given in Fig.

10a where the particles P1 and P2 occupy the boundaries between γ grains A/C and B/C respectively. The particle length of P1 and P2 is about 200 nm. The corresponding diffraction patterns of grains A and B in Figs. 10c and 10e reveal that the grains are oriented in two $\langle 100 \rangle$ variants of the γ lattice with a common $\langle 100 \rangle$ direction. In Figs. 10 d, f the combined diffraction patterns of the precipitates together with their respective γ matrix grains are shown. In both zone axis orientations $\{100\}$ type super-lattice reflections appear halfway between the fundamental $\{200\}$ reflections of the γ -matrix. The super-lattice reflections originate from the Perovskite structure of the Ti_3AlC precipitates that are aligned parallel to the γ matrix. The EDS spectrum of P1 shown in Fig. 10b confirms the presence of carbon in this precipitate. By comparison the intensity of the carbon peak in the surrounding grains A and C was considerably lower (not shown). P-type precipitates in the 1% alloy are located in grain boundaries comparable to the situation in the 0.75% alloy. It should be mentioned that in some small precipitates with P-type diffraction patterns no carbon is detected by EDS.

In the 0.5 % alloy diffraction patterns corresponding to the P-phase are observed occasionally in γ grains. Due to small size the corresponding precipitates could only be imaged by high-resolution. An example is given in Fig. 11 showing a γ grain in $[011]$ zone axis orientation that contains several strain lobes. The 'defects' that cause these strain lobes could be either lattice defects or the presence of a second phase. At close inspection 'defects' at the centre of the strain lobes can be classified as being orientated either parallel to $\{111\}$ planes or to extend along the $[100]$ direction of the γ grain. The former are lattice defects that are not of concern in the present study. An example of the latter type, imaged at high magnification, is shown in Fig. 12a. The arrow in Fig. 12a points to a boxed-in region of the crystal lattice that is distinguished from the surrounding matrix by new spatial frequencies in the Fast Fourier Transforms (FFT). At the bottom of the image diffractograms of the region around the defect (right) and of the undisturbed matrix (left) are shown. In the diffractogram of the defect region intensities are observed at spatial frequencies that correspond to (100) and $(0\bar{1}1)$ lattice planes of the Perovskite phase. For comparison no such intensities are observed in γ TiAl. In Fig. 12b the marked section of Fig. 12a is enlarged to illustrate the difference in contrast between the defect region and the matrix. It can be seen that in the defect region the shade of atoms in neighbouring vertical rows alternates between dark and bright (see arrows). For comparison all atom columns in the γ matrix have the same brightness values. The uniform brightness in case of the γ phase corresponds to the occupancy of atom columns with a mixture of Ti and Al atoms. In the case of the Perovskite

phase alternating atom columns are occupied by a mixture of Ti/Al atoms or exclusively by Ti atoms which leads to the observed contrast variation. Small insets in the top left corner and near the centre of the image in Fig. 12b represent the simulated high resolution images of γ -TiAl and P-type carbide respectively. Comparison shows that good agreement between experiment and simulation is obtained. The defect region is oriented along the [100] direction of the lattice and measures approximately 10 nm in length and 2.5 nm in width.

4. Discussion

The aim of this study was to monitor the occurrence and the character of carbides in ternary Ti-Al-Nb alloys containing different amounts of carbon. This is important because the exact solubility levels of carbon in high niobium containing TiAl alloys are still not well known. Also an influence of niobium towards increased carbon solubility is postulated in literature. Knowledge of the carbon concentration and of the processing parameters where carbon is either fully dissolved in the matrix phase or partly precipitated in the form of carbides will provide a better understanding of the carbide formation in such high niobium containing alloys. These studies are of extreme importance for the development of TiAl alloys because the mechanical properties at high temperature are strongly influenced by the presence of carbides. As a first step towards such studies we produced and characterized Ti-Al-Nb model alloys with homogenous chemical composition and carbon contents between 0 and 1%. The characterization of mechanical properties or the improvement of mechanical properties is a subsequent step that is not part of this article.

The microstructure of the processed Ti-45Al-5Nb-xC alloys ($x \leq 0 \leq 1$) consists of nearly equi-axed γ and α_2 grains. The γ and α_2 phase fractions remain constant over the carbon concentration range investigated, see section 3.1, 3.1.2. This is in agreement with observations by Chladil et. al who reported that the addition of C and Nb in Ti-45Al-5Nb-0.5C and in Ti-45Al-7.5Nb-(0.25, 0.5)C had no effect on the amount of α_2 and γ phase [8]. For comparison Cam et. al and Perdrix et. al find an increase in the amount of α_2 phase when C is added to binary Ti-Al alloys, which is attributed to the stabilizing effect of carbon on the α_2 phase [22, 29].

The size of γ and α_2 grains shows little dependence on carbon content, except for a small but noticeable minimum at 0.5 at% of C. Here both, γ and α_2 grains, are about 10% smaller than in the carbon free material and in alloys with higher carbon concentrations. This behavior

may be due to the solute drag effect of carbon atoms or may simply be the result of small deviations in the HIPing temperature. The contamination with other impurities is low (10-50 ppm N₂, 380-590 ppm O₂), however it is not understood why the solute drag effect would only act at the lowest carbon content. In literature a decrease in grain size with carbon addition was reported by Perdrix et al. for Ti-48Al produced by levitation melting. In this study on the binary alloy Ti-48Al with a fully lamellar microstructure Perdrix observed that a decrease in grain size coincides with the formation of H-type carbides at high carbon contents [22]. On the other hand no effect of carbon on the size of α_2 grains was found by Cha et. al in the alloys Ti-45Al-7.5Nb-(0; 0.5)C after oil quenching from the α region [25]. The authors explain their finding by the high starting temperature from which the alloys were quenched in combination with the full solubility of carbon in the α phase in this alloy.

The effect of carbon on lattice parameters and hardness is pronounced. Both increase linearly in the carbon concentration range between 0 and 0.75 at.-%. In contrast, hardness and lattice parameter remain constant between 0.75 and 1 % of C. At the same time HEXRD confirms the presence of H and P-type carbide phase in the carbon concentration range 0.75 - 1 % C but not at 0.50%. In the 0.5% C alloy third phase particles are difficult to observe, even by TEM, as is discussed in more detail below. Taken together the trends in hardness and lattice parameters and the presence of minor phases suggest that for carbon contents below 0.75 at.-% solid solution hardening is the predominant hardening mechanism. In this concentration range carbon is mainly hosted by the lattices of α_2 and γ phases resulting in the observed increase of lattice parameters and hardness with increasing carbon content. The precipitate phases identified at 0.75 and 1 at.-% C have no extra effect on hardness. The α_2 phase is known to host substantially more interstitial atoms than the γ phase, which is in agreement with the more pronounced increase in unit cell volume for the α_2 phase – especially in the range between 0 and 0.5 at% C [24]. Once the alloy's total solubility for carbon is reached, further addition of C leads to precipitation of carbides while the hardness remains constant. From our data the maximum carbon solubility of the alloy for carbon lies near 0.50 at.-%, but its exact value is not known yet.

A simultaneous increase in hardness and lattice parameters upon carbon addition has also been reported by Gerling et. al and Perdrix et. al [18, 22]. Gerling et. al measured a 14 % increase in hardness when 0.5 at% of carbon were added to Ti-45Al-5 Nb. This is in agreement with our results. In this study no precipitates were found by TEM or SANS, hence the hardness increase was explained by solid solution hardening. Perdrix et. al studied a

binary Ti-48Al alloy with carbon concentrations of up to 0.6 wt.-%. In the carbon concentration range between 20 – 1000 wt.-ppm the increase in hardness was attributed to carbon in solid solution. At higher carbon concentrations H-type carbides were detected by TEM and XRD and the hardness values leveled off.

Information on size, morphology and distribution of the detected precipitates is obtained from TEM and SEM investigations. H-type carbides are located at triple junctions and have a large size up to 1 μm in diameter. They have no orientation relationship with the surrounding grains. H-type carbides either form during HIPing at the boundaries of former primary grains or they are already present on the surface of the initial powder particles (see Fig. 7). From literature it is known that H-phase Ti_2AlC carbides form at higher temperatures than P-type Ti_3AlC carbides [14, 16] which supports the theory of a preferred position at boundaries of primary grains. XRD measurements of the powder before HIPing did not provide evidence for the presence of carbides. Therefore the hypothesis that the powder particles used for HIPing are covered by carbon rich particles is rejected.

The number of H-type precipitates decreases drastically as the carbon content is lowered from 1 at.-% to 0.75 at.-% (compare Figs. 7, 8). At the same time the number of P-type precipitates identified by TEM is higher in the 0.75% alloy than in the 1% alloy, where only a few P-type precipitates were found. These SEM and TEM observations are in agreement with the relative intensities of both phases in the HEXRD spectra in Fig. 3b. P- phase particles are mainly located at boundaries of γ grains as illustrated in Fig. 10. The P-type precipitates hold a parallel orientation relationship with the γ matrix as illustrated in Fig.10 and as described in literature [16].

In the 0.5% alloy no minority phase is detected by HEXRD and only few very small regions are identified by TEM that give rise to the typical P-type diffraction patterns. In Figs. 11 and 12 images of such P-phase containing regions are shown together with a diffractogram that confirms the Perovskite structure. The P-phase regions are located within γ -grains and have fuzzy boundaries that cannot be outlined clearly. The shape is elongated in [100] direction which differs from literature reports. Nemotho and Christoph reported P-type particles in γ grains after long annealing times. The rod like precipitates extend along the [001] c-direction of the γ matrix [16, 17]. The finding of P-type regions within γ grains may be explained considering the atomic arrangement of Ti and Al atoms and the occurrence of concentration fluctuations during cooling. The two phases γ -TiAl and Ti_3AlC differ in Ti content and in the ordering of Ti and Al atoms onto their specific lattice sites. In γ -TiAl (in

fcc notation) Al atoms occupy the top and bottom layer of an fcc unit cell. Ti atoms reside on the remaining face centres, forming a Ti-layer at $z=0.5$. In the cubic Perovskite unit cell of Ti_3AlC , corner sites are occupied by Al atoms, while Ti atoms reside on all face centres. Carbon atoms occupy the body centred position. This arrangement provides the preferred octahedral coordination of carbon atoms with Ti [12, 30]. Therefore it is plausible that P-phase Ti_3AlC forms where the appropriate environment is provided in the presence of carbon. For example the continued $\alpha \rightarrow \gamma (+\alpha_2)$ transformation during cooling from HIPing temperature may lead to super saturation of γ with carbon and Ti, thereby providing such an environment. The small size, ill-defined boundaries and the atypical extension along [100] direction suggest that these small P-type regions are seeds rather than well defined inclusions. Further studies of these P-type regions are however beyond the scope of this paper. In literature a carbon solubility in γ phase of 0.25 at.-% and values ≥ 1 at.% for the α_2 phase (possibly up to 1.5 %) have been reported [23]. Applied to the current case of the 0.5 % alloy this translates into a situation where full solubility of carbon could exist, or where full solubility is just exceeded in some places. According to a rough estimate, considering 83 vol.-% of γ , 17 vol.-% of α_2 (from section 3.1.2) and a solubility of 1.5 at.-% C in α_2 , all carbon should be in solution. For comparison the finding of carbides in grain boundaries in the 0.75% alloy suggests that the carbon solubility in γ -grains is saturated and excess carbon is squeezed out of the γ -lattice into the grain boundary where precipitates are formed.

Indirect evidence for the minute amount of P-phase in the 0.5 % alloy is identified in the HEXRD data. Here only about 0.1 vol.-% of P-phase is found in the 1% alloy. For the 0.5 % alloy no P-phase peaks are visible. Consequently an even smaller, negligible amount of P-phase than 0.1 vol.-% should be present in the 0.5 % alloy. Therefore the occurrence of P-phase precipitates in the as HIPed state of the 0.5% alloy is not a typical feature but rather an exception. This is in agreement with literature reports on this alloy composition, where no carbides have been detected by atom probe or SANS measurements [19, 23]. Similarly, no carbides were found in the high Nb containing TiAl alloy, Ti-45Al-7.5Nb-0.5C, processed above 930°C for a short time [25]. On the other hand a high density of P-type precipitates was reported for a binary Ti-48.5Al alloy with 0.37 at.-% of carbon subjected to an ageing heat treatment [17, 26]. Comparison of these findings indicates that Nb may either increase the solubility for carbon in TiAl alloys or that it renders the kinetics for the formation of carbides sluggish at this low carbon concentration.

5. Conclusions

In Ti-45Al-5Nb-xC ($0 \leq x \leq 0.75$) alloys produced by HIPing from powders a strong effect of carbon on macro hardness and on lattice parameters has been observed. In this carbon concentration range only very few precipitates are observed in the HIPed material. At higher carbon contents ($0.75 \leq x \leq 1$ at.-%) many precipitates of H and P type carbides are observed, but the measured macro-hardness remains constant. Once a considerable number of precipitates have formed at 0.75 at.-% C the lattice parameters decrease slightly. In general, P-type carbides form at lower carbon content, while H-type carbides form at higher carbon levels. The preferred locations of P and H-type carbides at γ grain boundaries or boundaries of primary grains respectively indicate that they form by separate mechanisms, possibly during different stages of the HIPing process. Our results suggest that in the present case solid solution hardening is the active mechanism for the observed increase in hardness.

REFERENCES

- [1] A. Stark, Textur- und Gefügeentwicklung bei der thermomechanischen Umformung Nb-reicher Gamma-TiAl-Basislegierungen, in: T.U. Zugl.: Hamburg-Harburg, Institut für Werkstoffphysik und -technologie, Diss., 2009 (Ed.), Shaker, Aachen, Germany, 2010.
- [2] Y.L. Hao, D.S. Xu, Y.Y. Cui, R. Yang, D. Li, The site occupancies of alloying elements in TiAl and Ti₃Al alloys *Acta Materialia*, 47 (1999) 1129-1139.
- [3] G.L. Chen, X.J. Xu, Z.K. Teng, Y.L. Wang, J.P. Lin, Microsegregation in high Nb containing alloy ingots beyond laboratory scale, *Intermetallics*, 15 (2007) 625-631.
- [4] S. Gebhard, F. Pyczak, M. Goken, Microstructural and micromechanical characterisation of TiAl alloys using atomic force microscopy and nanoindentation, *Materials Science and Engineering a-Structural Materials Properties Microstructure and Processing*, 523 (2009) 235-241.
- [5] Z.C. Liu, J.P. Lin, S.J. Li, G.L. Chen, Effects of Nb and Al on the microstructures and mechanical properties of high Nb containing TiAl base alloys, *Intermetallics*, 10 (2002) 653-659.
- [6] H. Jabbar, J.-P. Monchoux, F. Houdellier, M. Dollé, F.-P. Schimansky, F. Pyczak, M. Thomas, A. Couret, Microstructure and mechanical properties of high niobium containing TiAl alloys elaborated by spark plasma sintering, *Intermetallics*, 18 (2010) 23112-22321.
- [7] H.F. Chladil, H. Clemens, M. Takeyama, E. Kozeschnik, A. Bartels, R. Gerling, S. Kremmer, On the influence of Nb on the transition temperatures of titanium aluminides, *Advanced Intermetallic-Based Alloys*, 980 (2007) 371-376.
- [8] H.F. Chladil, H. Clemens, H. Leitner, A. Bartels, R. Gerling, F.-P. Schimansky, S. Kremmer, Phase transformations in high niobium and carbon containing γ -TiAl based alloys, *Intermetallics*, 14 (2006) 1194-1198.
- [9] Y. Wu, Y.W. Park, H.S. Park, S.K. Hwang, Microstructural development of indirect-extruded TiAl-Mn-Mo-C intermetallic alloys during ageing, *Materials Science & Engineering A*, A347 (2003) 171-179.
- [10] Z.J. Lin, M.J. Zhuo, Y.C. Zhuo, M.S. Li, J.Y. Wang, Microstructural characterization of layered ternary Ti₂AlC, *Acta Materialia*, 54 (2006) 1009-1015.
- [11] J. Emmerlich, D. Music, A. Houben, R. Dronskowski, J.M. Schneider, Systematic study on the pressure dependence of M₂AlC phases (M = Ti, V, Cr, Zr, Nb, Mo, Hf, Ta, W), *Physical Review B*, 76 (2007) 224111.

- [12] V. Kanchana, Mechanical Properties of Ti_3AlX ($X= C, N$) : Ab initio study, EPL A Letters Journal Exploring the Frontiers of Physics, 87 (2009) 26006.
- [13] M.A. Pfietzka, J.C. Schuster, Summary of Constitutional Data on the Aluminum-Carbon-Titanium System, Journal of Phase Equilibria, 15 (1994) 392-400.
- [14] S. Chen, P.A. Beaven, R. Wagner, Carbide Precipitation in γ -TiAl Alloys, Scripta Metallurgica et Materialia, 26 (1992) 1205-1210.
- [15] P.I. Gouma, S.J. Davey, M.H. Loretto Microstructure and mechanical properties of a TiAl-based powder alloy containing carbon, Materials Science & Engineering A, A 241 (1998) 151- 158.
- [16] W.H. Tian, M. Nemoto, Effect of carbon addition on the microstructures and mechanical properties of γ -TiAl alloys, Intermetallics, 5 (1997) 237-244.
- [17] U. Christoph, F. Appel, R. Wagner, Dislocation dynamics in carbon-doped titanium aluminide alloys, Materials Science & Engineering A239-240 (1997) 39-45.
- [18] R. Gerling, F.P. Schimansky, A. Stark, A. Bartels, H. Kestler, L. Cha, C. Scheu, H. Clemens, Microstructure and mechanical properties of Ti 45Al 5Nb + (0-0.5C) sheets, Intermetallics, 16 (2008) 689-697.
- [19] P. Staron, F.-P. Schimansky, C. Scheu, H. Clemens, SANS study of carbon addition in Ti-45Al-5Nb, in: B. Bewlay, M. Palm, S. Kumar, K. Yoshimi (Eds.) Fall Meeting of the Materials Research Society, Mater. Res. Soc. Proc., Boston, 2010, pp. 195-200.
- [20] J.D. Whittenberger, R. Ray, Deformation properties of $AlTi_2C$ particle containing Ti-46Al-2Cr-2Nb alloys at 1000 to 1200 K, Scripta Metallurgica et Materialia, 33 (1995) 1505-1512.
- [21] B.D. Worth, J.W. Jones, J.E. Allison, Creep Deformation in Near- γ TiAl : II. Influence of Carbon on Creep Deformation in Ti-48Al-0.3C, Metallurgical and Materials Transactions A, 26 A (1995) 2961-2972.
- [22] F. Perdrix, M.-F. Trichet, J.-L. Bonnentien, M. Cornet, J. Bigot, Relationships between interstitial content, microstructure and mechanical properties in fully lamellar Ti-48Al alloys, with special reference to carbon, Intermetallics, 9 (2001) 807-815.
- [23] C. Scheu, E. Stergar, M. Schober, L. Cha, H. Clemens, A. Bartels, F.P. Schimansky, A. Cerezo, High carbon solubility in a gamma-TiAl-based Ti-45Al-5Nb-0.5C alloy and its effect on hardening, Acta Materialia, 57 (2009) 1504-1511.
- [24] A. Menand, A. Huguet, Nerac-Partaix, Interstitial Solubility in γ and α_2 Phases of TiAl-Based Alloys, Acta materialia, 44 (1996) 4729-4737.

- [25] L. Cha, C. Scheu, H. Clemens, H.F. Chladil, G. Dehm, R. Gerling, A. Bartels, Nanometer-scaled lamellar microstructures in Ti-45Al-7.5Nb-(0; 0.5)C alloys and their influence on hardness, *Intermetallics*, 16 (2008) 868-875.
- [26] P. Staron, U. Christoph, F. Appel, H. Clemens, SANS investigation of precipitation hardening of two-phase γ -TiAl alloys, *Applied Physics A*, 74 (2002) 1162-1165.
- [27] H.S. Park, S.W. Nam, N.J. Kim, S.K. Hwang, Refinement of the lamellar structure in TiAl-based intermetallic compound by addition of carbon, *Scripta Materialia*, 41 (1999) 1197-1203.
- [28] R. Gerling, H. Clemens, F.P. Schimansky, Powder Metallurgical Processing of Intermetallic Gamma Titanium Aluminides, *Advanced Engineering Materials*, 6 (2004) 23-38.
- [29] G. Cam, H.M. Flower, D.R.F. West, The Alloying of Titanium Aluminides with Carbon, in: *Materials Research Society Symposium Proceedings*, Materials Research Society, Boston, MA, USA, 1989, pp. 663-668.
- [30] J.C. Schuster, H. Nowotny, C. Vaccaro, The Ternary Systems :Cr-Al-C, V-Al-C, and Ti-Al-C and the Behavior of H-Phases (M_2AlC), *Journal of Solid State Chemistry*, 32 (1980) 213-219.

Figure captions

Fig.1. Microstructure of Ti-45Al-5Nb-0.5C observed by SEM (BSE mode). (a) large lamellar colonies, (b) globular α_2 and γ grains, (c) ill-defined lamellar colonies.

Fig.2. Relative volume fraction of γ phase in Ti-45Al-5Nb-xC alloys. The remaining fraction is assumed to be α_2 phase. Comparison of the results obtained by different methods does not reveal a clear trend between phase fraction and carbon concentration.

Fig.3. HEXRD pattern of Ti45Al-5Nb-xC alloys. Scattering vector $|q| = 2\pi/d = 2\pi \cdot (2\sin\theta/\lambda)$. (a) Overview with marks for peak positions of γ , α_2 , P-phase and H-phase. The rectangular sections indicate the angular range enlarged in Figs. 3b, c. (b.) Enlarged section showing diffracted intensity of P- and H-phase in the 0.75 and 1 % alloy. (c) Section of the diffraction pattern illustrating the peak shift due to the lattice expansion with increasing C contents.

Fig.4. Change in unit cell volume with carbon addition (the maximum error is lower than +/- 0.025 %). Both phases have the largest increase in unit cell volume at 0.75 at.-% of carbon.

Fig.5. Trend in macro hardness (HV 20) with addition of carbon in Ti-45Al-5Nb-xC alloys.

Fig 6. TEM and SEM images of Ti-45Al-5Nb-1C : (a) image taken at low magnification showing dissolution of precipitates near the edge of the TEM foil. (b) image of a precipitate that is partially dissolved at the center. (c.) SEM Image showing several precipitates at grain boundaries. An EDS line scan across one particle marked in the image illustrates elevated carbon content in the precipitate.

Fig. 7. SEM images of Ti-45Al-5Nb-1C. (a.) SE image showing the position of former H-type carbides at the boundary of larger primary grains. (b.) BSE image of the same area showing that smaller α_2 and γ grains cover the area enclosed by larger primary grains in (a).

Fig. 8. SE image of Ti-45Al-5Nb-0.75C. The number of etch pits indicating the position of former carbides (see arrows) is much smaller than in the 1% alloy.

Fig. 9. Ti-45Al-5Nb-0.75C: Corresponding bright field image, [100](002) dark field image and diffraction pattern of H-type particle.

Fig. 10. Ti-45Al-5Nb-0.75C : a.) Precipitates P1, P2 located in grain boundary between γ grains A, B, and C. b.) EDS spectrum of particle P1 illustrating presence of carbon. c.) Diffraction pattern of grain A, d.) Combined diffraction pattern of precipitate P1 and grain A. e.) diffraction pattern of grain B. f.) combined diffraction pattern of particle P2 and grain B.

Fig. 11 : Ti-45Al-5Nb-0.5C : Image and diffraction pattern of γ grain in near [011] zone axis orientation showing several strain lobes.

Fig 12 : Ti-45Al-5Nb-0.5C , enlarged section of a strain lobe in Fig. 11. a.) High resolution image showing the lattice around a strain lobe together with FFT of the region of the defect (right) and the matrix (left). b.) The inset marked in a.) at higher magnification. The contrast variation between matrix and defect is compared to simulated high resolution images for the γ - matrix (marked rectangle top left) and the P-type Ti_3AlC phase (marked rectangle near center).

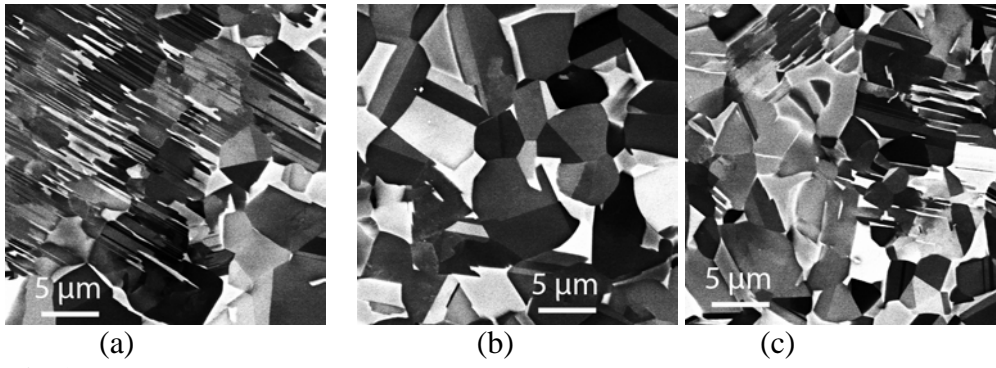


Fig.1

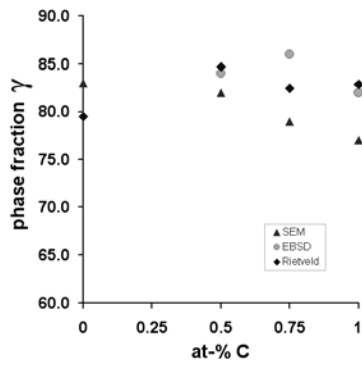


Fig.2

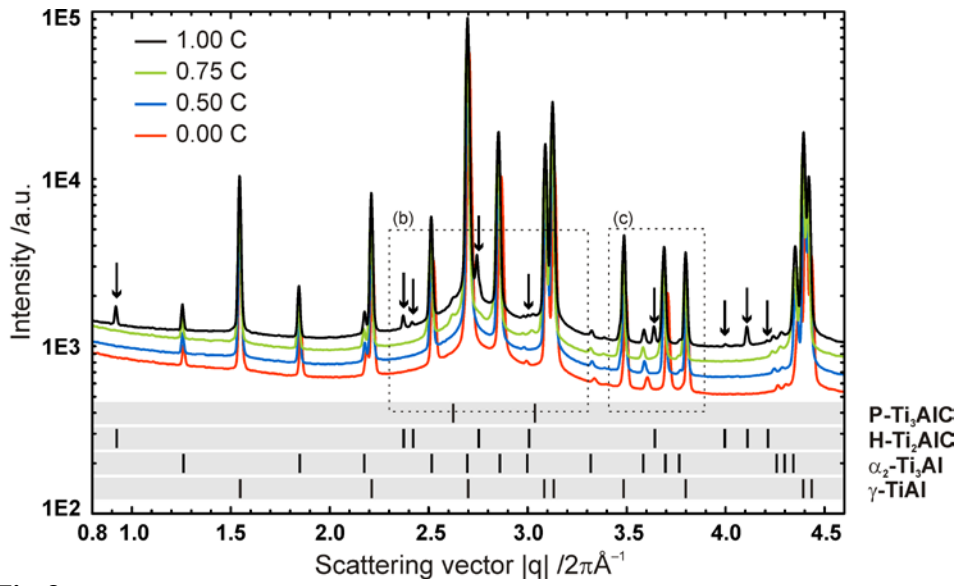


Fig 3a

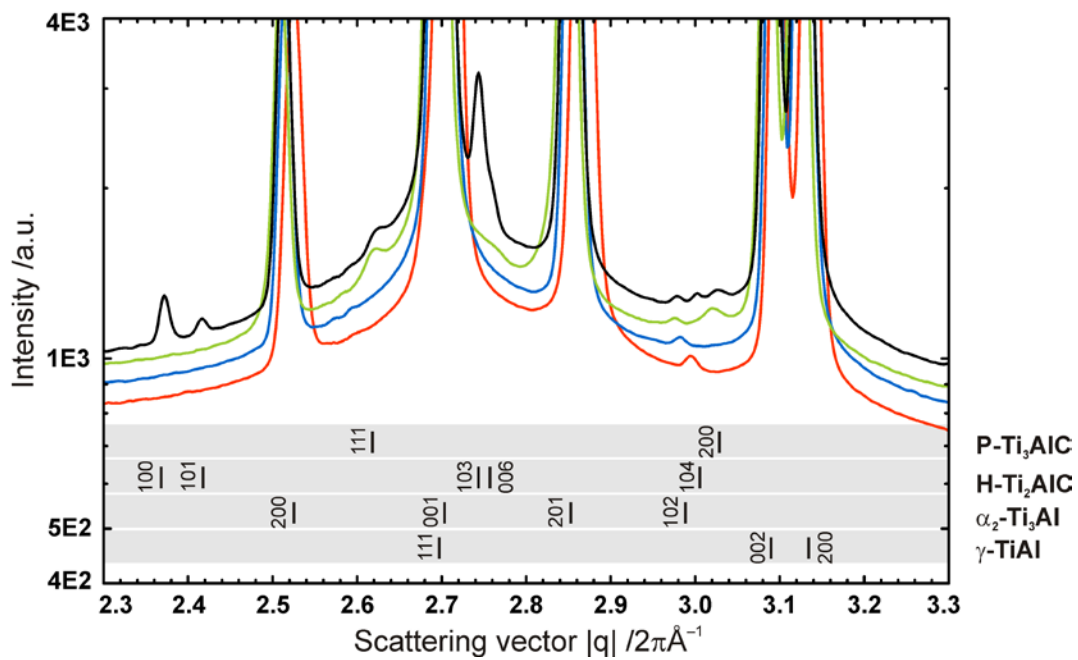


Fig 3b

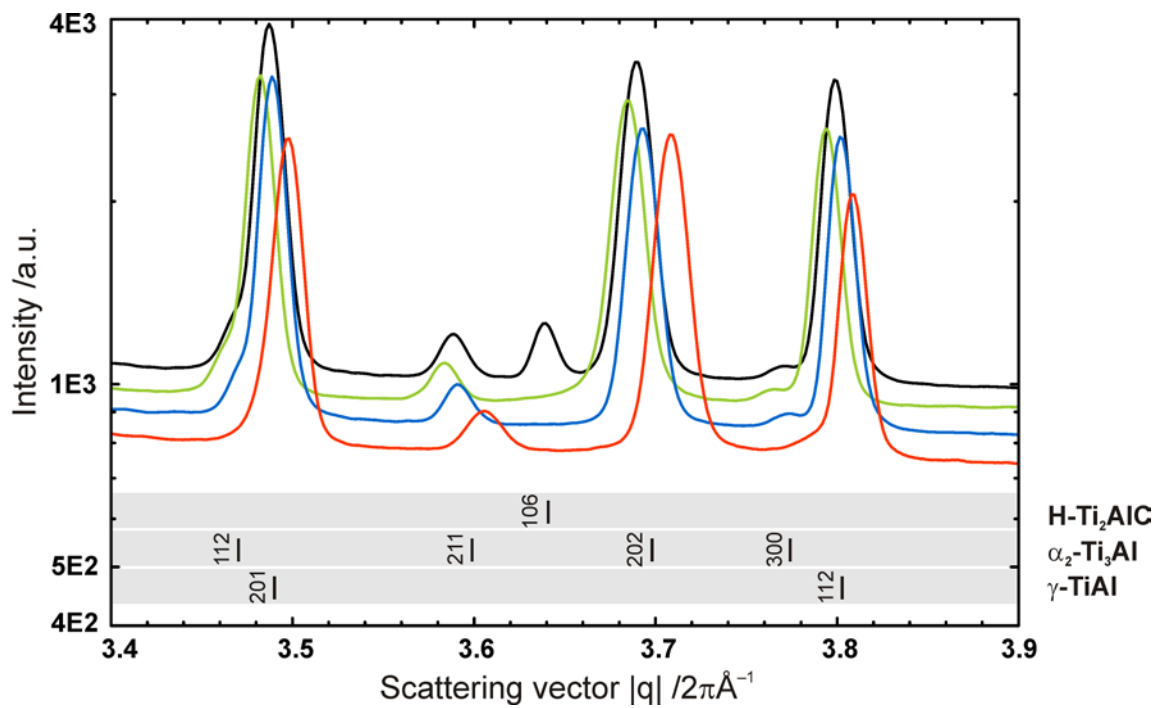


Fig 3c

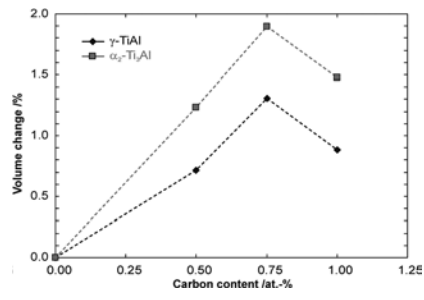


Fig. 4

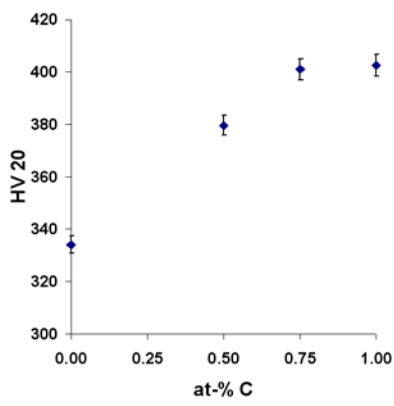


Fig. 5

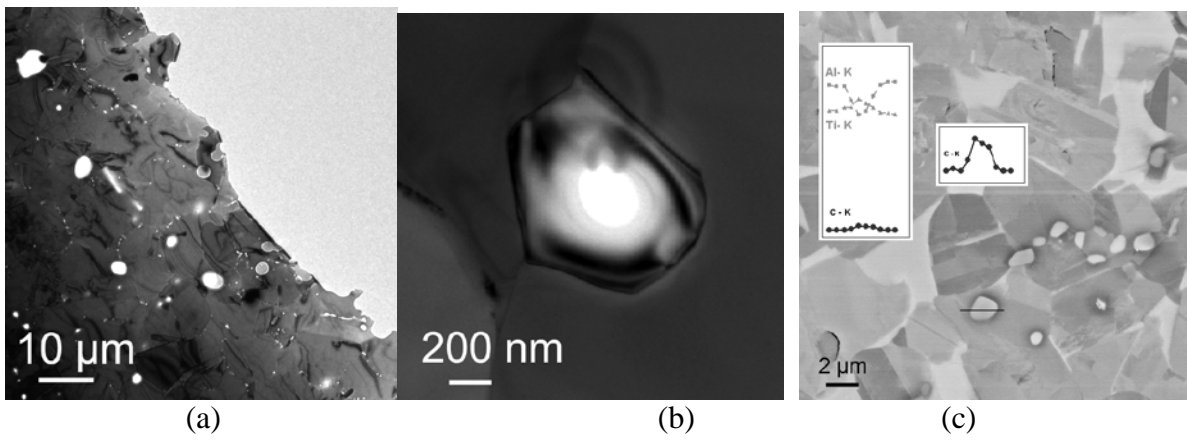


Fig. 6

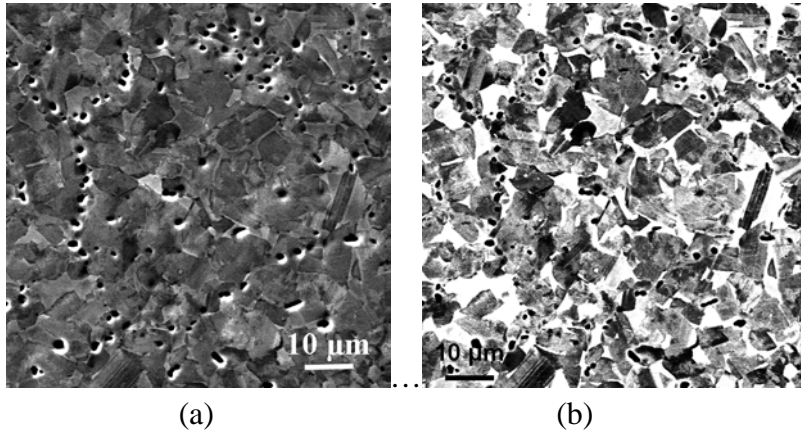


Fig. 7.

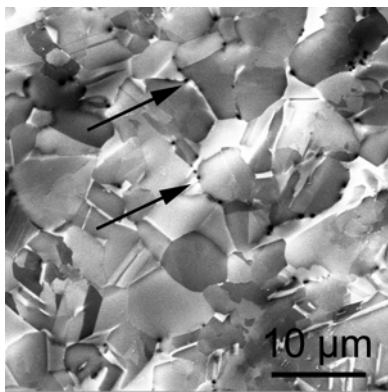


Fig. 8.

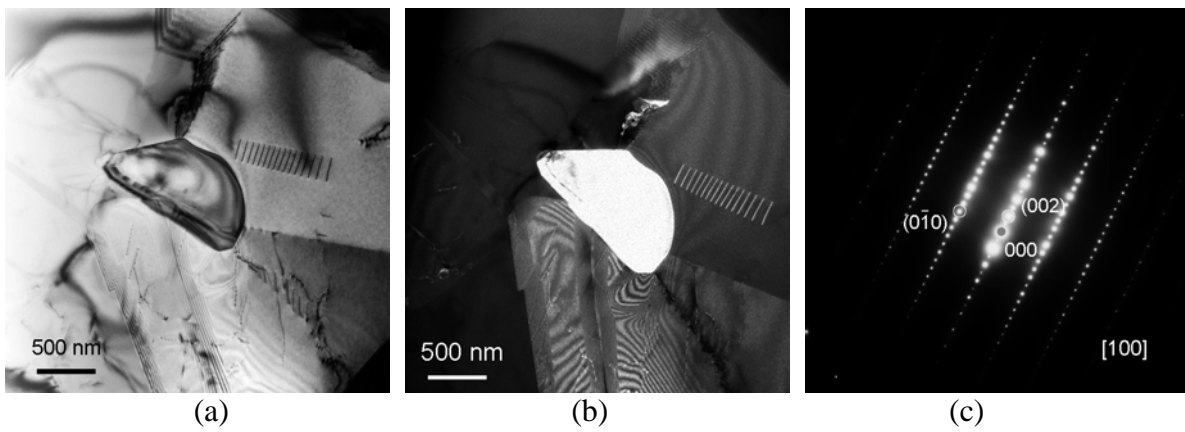


Fig. 9

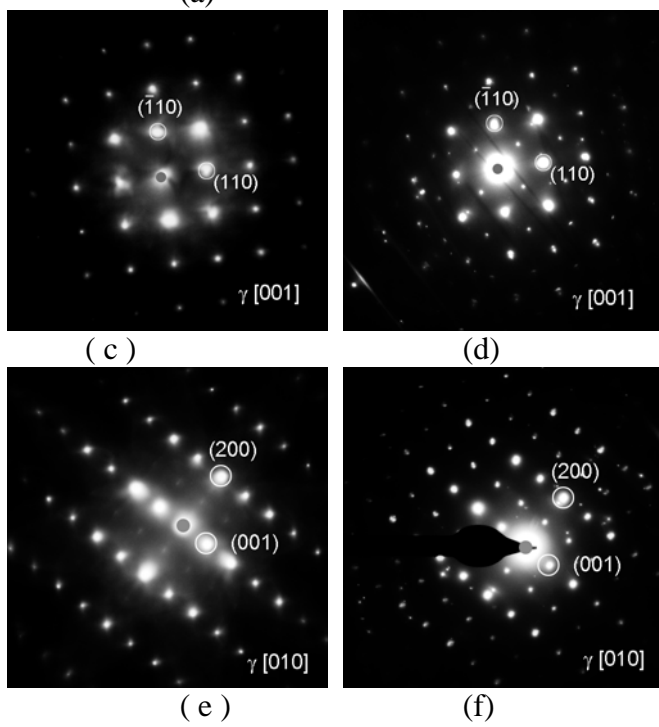
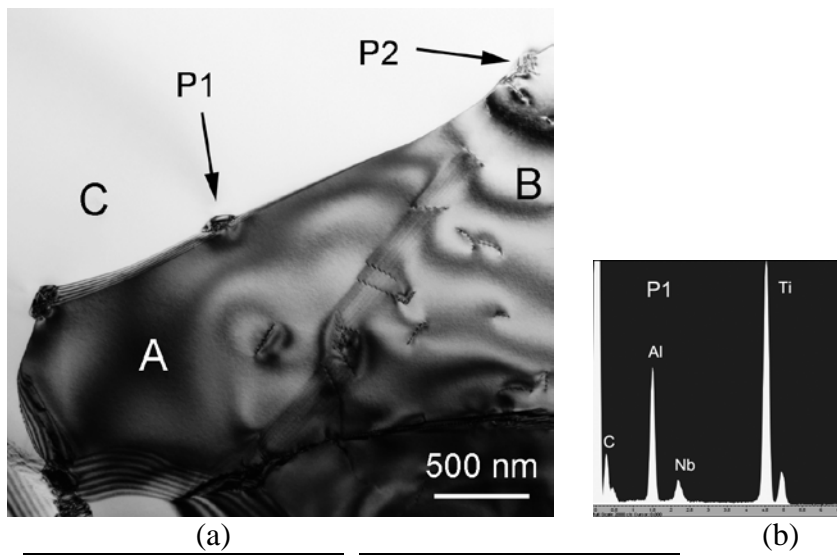


Fig. 10

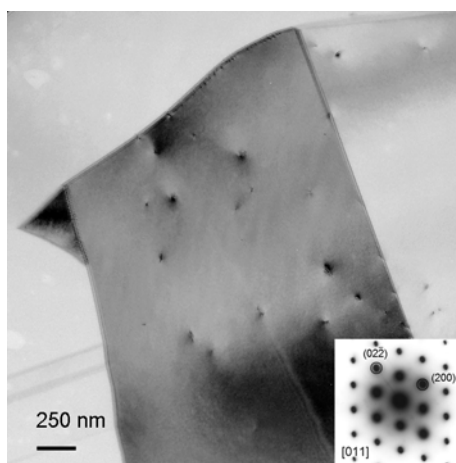
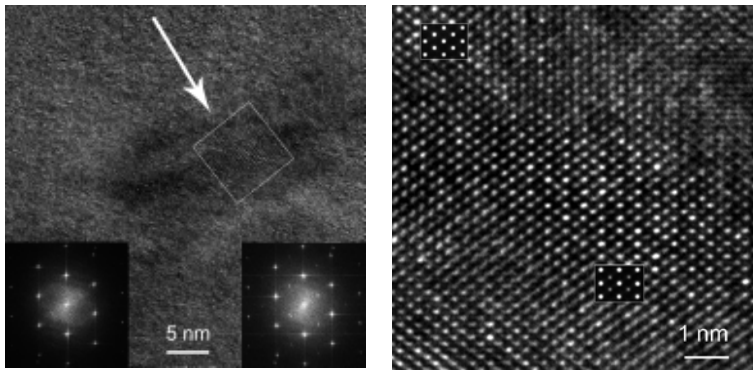


Fig. 11



(a)

(b)

Fig. 12
